

# Search for Axion-Like Particles in High-Magnetic-Field Pulsars with NICER

Yen-Jhen Liu and Yi Yang

*Department of Physics, National Cheng Kung University, Tainan, Taiwan (ROC) and  
Institute of Physics, Academia Sinica, Taiwan (ROC)*

(Dated: February 10, 2026)

Axion-like particles (ALPs) can couple to photons in strong magnetic fields, producing characteristic fluctuations in X-ray spectra. Using data from NASA's Neutron Star Interior Composition EXplorer (NICER), we analyzed three pulsars, PSR J2229+6114, PSR J1849-0001, and PSR B0531+21, to search for such features. Each spectrum was modeled with a sliding-window power-law fitting method to identify local deviations from the smooth continuum. From these analyses, we derived constraints on the axion-photon coupling constant  $g_{a\gamma\gamma}$  from dipole and quadrupole magnetic field distribution assumption, obtaining upper limits in the range  $10^{-10} - 10^{-13} GeV^{-1}$  within the 0.8–10 keV mass region.

## I. INTRODUCTION

The Standard Model (SM) of particle physics has achieved remarkable experimental success over the past several decades, yet several unresolved issues remain, among which the strong CP problem in quantum chromodynamics (QCD) is particularly compelling[1–3]. This problem arises from the theoretically allowed but experimentally unobserved CP-violating term in the QCD Lagrangian:

$$\mathcal{L}_{\text{CP-vio}} = \frac{\alpha_s}{4\pi} \theta \text{Tr} \left( G_{\mu\nu} \tilde{G}^{\mu\nu} \right) \quad (1)$$

where  $G_{\mu\nu}$  is the gluon field strength tensor and  $\tilde{G}^{\mu\nu}$  its dual. To resolve this, the Peccei-Quinn mechanism was proposed, giving rise to the axion—a pseudoscalar Nambu-Goldstone boson. Extensions of the SM predict more general axion-like particles (ALPs) that couple to photons via

$$\mathcal{L}_{a\gamma\gamma} = -\frac{1}{4} g_{a\gamma\gamma} a F_{\mu\nu} \tilde{F}^{\mu\nu} = g_{a\gamma\gamma} a \mathbf{E} \cdot \mathbf{B}, \quad (2)$$

where  $a$  is the axion field,  $g_{a\gamma\gamma}$  is the coupling constant,  $F$  and  $\tilde{F}$  are the electromagnetic field-strength tensor and its dual,  $\mathbf{E}$  and  $\mathbf{B}$  are the electric field and magnetic field. For an electromagnetic wave, the interaction specifically requires the electric field component parallel to the external magnetic field ( $E_{\parallel} B_{\perp}$ ). This property enables photon-to-ALPs conversion in strong magnetic fields; the resulting photon-ALP conversion probability in a magnetic field is determined by the mixing of the photon and ALP states as they propagate through the magnetosphere [4, 5].

ALPs are probed by experiments targeting either non-relativistic or relativistic regimes. Non-relativistic ALPs, with low velocities are primary dark matter candidates, detected by haloscopes like Axion Dark Matter eXperiment (ADMX) and Taiwan Axion Search Experiment with a Haloscope (TASEH) [6–10] in resonant cavity as well as constrained by cosmological evolution like Big Bang Nucleosynthesis (BBN) [11] and cosmic background [12] and so on. Relativistic ALPs are explored by helioscopes like CERN Axion Solar Telescope (CAST) [13], by

light-shining-through-walls (LSW) experiments like Any Light Particle Search (ALPS)[14], and by pulsarscope studies [15].

Pulsars are uniquely powerful source for axion-like particle research due to their extreme magnetic fields. Young rotation-powered pulsars typically have surface dipole magnetic fields of  $10^{11}$ – $10^{13}$  G, far stronger than any achievable in terrestrial experiments and significantly higher than those of millisecond pulsars (MLPs). Such intense fields greatly enhance the probability of photon-ALP conversion, which may result to fluctuation features in their X-ray spectra.

In this work we probe possible fluctuation in pulsar spectra arising from photon-ALPs conversion in their magnetospheres. Focusing on the soft X-Ray band accessible to NASA's Neutron Star Interior Composition Explorer (NICER, 0.3-12 keV), we exclude the non-relativistic dark-matter ALP regime and instead explore the relativistic regime. This enables us to improve the constraints on coupling constant  $g_{a\gamma\gamma}$  within a refined parameter space compared to previous results[16–18].

## II. FORMULA

The evolution of the coupled photon-ALP system as it traverses the pulsar magnetosphere can be described by a Schrödinger-like equation:

$$-i \frac{d}{dz} \Psi(z) = \mathcal{M} \Psi(z), \quad \Psi(z) = \begin{pmatrix} A_{\perp}(z) \\ a(z) \end{pmatrix} \quad (3)$$

where  $A_{\perp}(z)$  and  $a(z)$  represent the photon and ALP field amplitudes with path length  $z$ , respectively. The mixing matrix  $\mathcal{M}$  accounts for the interaction between the states:

$$\mathcal{M} = \omega \mathbb{1} + \begin{pmatrix} \Delta_{\gamma}(z) & \Delta_{a\gamma}(z) \\ \Delta_{a\gamma}(z) & \Delta_a(z) \end{pmatrix} \quad (4)$$

In this framework,  $\omega$  is the oscillation frequency in vacuum,  $\Delta_{\gamma}$  and  $\Delta_a$  are the refractive indices for photons and ALPs, and  $\Delta_{a\gamma}(z) = \frac{1}{2} g_{a\gamma\gamma} B_{\perp}(z)$  represents the interaction strength mediated by the transverse magnetic field.

To quantify the photon-to-ALP conversion, we consider the probability  $\mathcal{P}(\gamma \rightarrow a)$  of a photon emitted from the stellar surface ( $z = 0$ ) converting into an ALP as it propagates to infinity. Following standard magnetospheric emission models, we assume the X-ray photons originate at or near the surface, where the dense stellar interior is opaque to X-ray propagation. The momentum transfer between the photon and ALP is given by  $q = \frac{m_a^2 - \omega_{pl}^2}{2E}$ , where the  $\omega_{pl}$  is the plasma frequency. In the small-mixing limit ( $q \approx 0$ ), where the conversion efficiency is low, the probability can be expressed in an integral form:

$$\begin{aligned} \mathcal{P}(\gamma \rightarrow a) &= \left| \int_0^\infty \Delta_{a\gamma}(z) e^{iqz} dz \right|^2 \\ &= \left| \int_0^\infty \frac{1}{2} g_{a\gamma\gamma} B_\perp(z) e^{iqz} dz \right|^2 \\ &\approx \left| \int_0^\infty \frac{1}{2} g_{a\gamma\gamma} B_\perp(z) dz \right|^2 \text{ if } q \approx 0. \end{aligned} \quad (5)$$

For a standard dipole distribution, the transverse magnetic field component is  $B_\perp(r) = B(r) \sin \theta$ , where  $\theta$  is the angle between the magnetic axis and the line of sight. The field scales as  $1/r^3$ . By substituting  $r = R_{\text{NS}} + z$ , where  $R_{\text{NS}}$  is the neutron star radius, we anchor the coordinate system to the emission site at the surface ( $z = 0$ ). Under this approximation, the integral simplifies to a clean analytical form:

$$\begin{aligned} \mathcal{P}(\gamma \rightarrow a) &= \left| \frac{1}{2} g_{a\gamma\gamma} \sin \theta B_0 R_{\text{NS}}^3 \int_0^\infty \frac{1}{(R_{\text{NS}} + z)^3} dz \right|^2 \\ &= \left| \frac{1}{4} g_{a\gamma\gamma} \sin \theta B_0 R_{\text{NS}} \right|^2. \end{aligned} \quad (6)$$

Beyond the dipole assumption, we can expand this to a general multipole form. Since there is no free current outside the neutron star, the magnetic potential  $\Phi_M$  satisfies Laplace's equation,  $\nabla^2 \Phi_M = 0$ . In spherical coordinates, requiring the field to vanish at infinity implies a radial scaling of  $B \propto 1/r^{l+2}$  for a multipole of order  $l$ :

$$B_\perp(r, \theta) = B_0 \left( \frac{R_{\text{NS}}}{r} \right)^{l+2} \sin \theta \quad (7)$$

Using this generalized field in the conversion integral yields the final probability for any multipole order  $l$ :

$$\mathcal{P}(\gamma \rightarrow a) = \left| \frac{1}{2(l+1)} g_{a\gamma\gamma} \sin \theta B_0 R_{\text{NS}} \right|^2. \quad (8)$$

This generalized result allows us to evaluate the sensitivity of our constraints to different magnetospheric models, with  $l = 1$  representing a standard dipole field and  $l = 2$  representing the quadrupole field.

### III. ANALYSIS

We analyzed the soft X-ray spectra of three rotation-powered pulsars—PSR J2229+6114, PSR J1849-0001, and PSR B0531+21—using data from NASA's NICER mission [19]. All spectra (see the Table 1 in Appendix) in this work were processed using the HEASoft version 6.35.2 and NICERDAS version 11 pipeline, with event filtering performed via NICERL2 and spectral extraction through NICERL3-spect. For our background subtraction, we utilized the "3c50" empirical model[20]. All of the spectra show in Fig. 1, the yellow banding region means the fit range we used. Following the magnetospheric emission models for young pulsars [21, 22], we assume the X-ray photons in the 0.8–10 keV range originate from the polar cap or the near-surface vacuum gaps. Because these emission heights are negligible compared to the conversion path length, and given the star's opacity to X-rays, we define the starting point of our integral at the neutron star surface.

To identify potential spectral fluctuations indicative of photon-ALP conversion, each pulsar's continuum was modeled with an absorbed power-law function:  $F(E) = AE^{-\Gamma}$ . A sliding-window fitting approach was applied to detect localized deviations from this smooth baseline. We used a window width of 4 bins for energies below 2 keV and increased this to 10 bins for higher energies to account for decreasing photon statistics. Due to the overlapping nature of the windows, each energy bin is included in multiple fits and thus associated with more than one set of best-fit parameters. To determine the most representative local fit, we adopted the minimum  $\chi^2$  criterion, selecting for each energy bin the fit corresponding to the lowest reduced  $\chi^2$  value among all overlapping windows, all calculation are calculated at the 95% confidence level. The statistical significance of deviations between the data and our baseline model was quantified using the "pull" ( $z_i$ ):

$$z_i = \frac{y_{\text{data},i} - y_{\text{model},i}}{\sigma_i s_i}, \quad s_i = \sqrt{\frac{\chi^2}{d.o.f}} \quad (9)$$

where  $s_i$  is the scaling factor from the local fit. From this, we calculated a two-tailed Gaussian probability

$$p_{\text{two-tailed},i} = 2[1 - \Phi(|z_i|)] \quad (10)$$

to determine the likelihood that a deviation arose from random noise, where  $\Phi$  is the Cumulative Distribution Function, which is used to represent random fluctuation would push the measurement at least this far away from prediction. Finally, we defined an empirical conversion probability,  $P_{\text{conversion},i} = 1 - p_{\text{two-tailed},i}$ , to represent the chance that an observed fluctuation is not consistent with random noise and could potentially be interpreted as a photon-axion conversion signature.

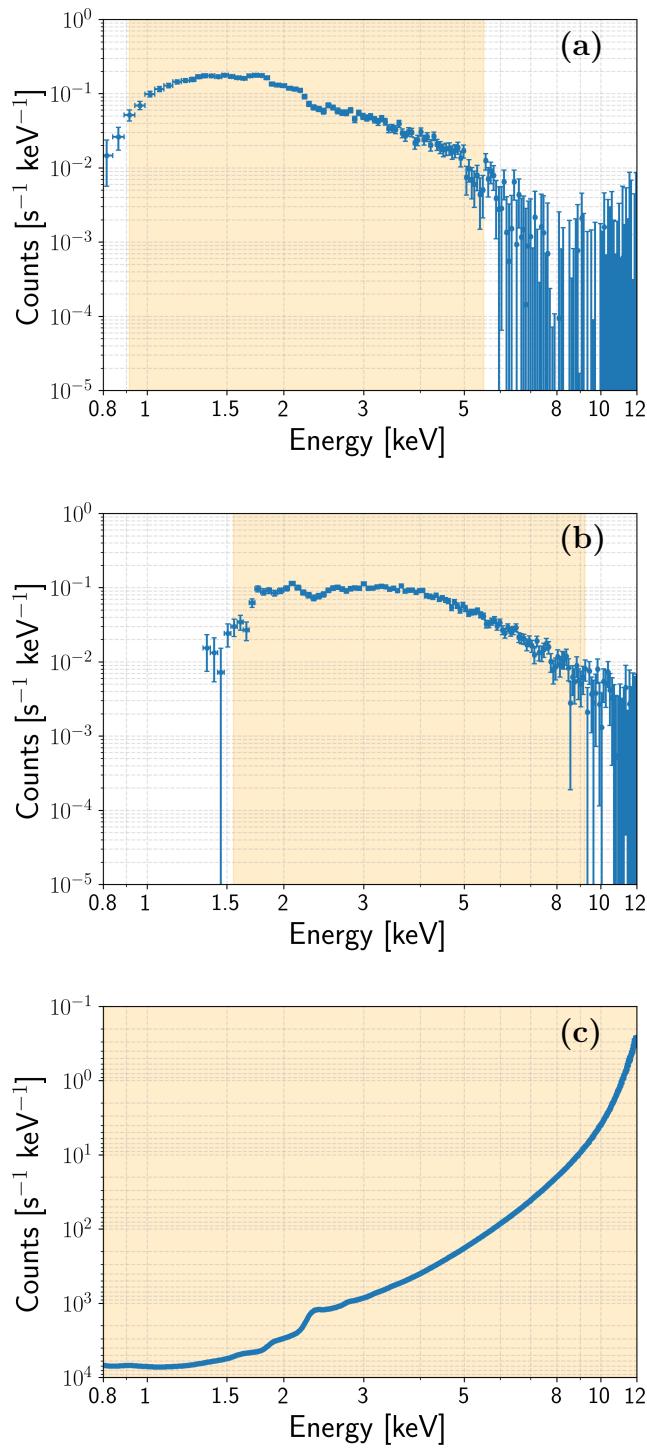


FIG. 1. The merged Pulsar spectrum for (a) J2229+6114, (b) J1849-0001, and (c) B0531+21 with 3c50 background model subtraction, the colored band means the energy range we used to fit.

#### IV. RESULT

For a typical pulsar radius between 10 to 13 km, we take  $R_{\text{NS}} = 13$  km when estimating the conversion scale.

To refine our constraints, we incorporated pulsar-specific geometry by assuming tilt angles ( $\theta$ ) based on existing multi-wavelength research. We adopted  $\theta \approx 60^\circ$  for PSR B0531+21 based on its torus-jet morphology,  $\theta \approx 45^\circ$  for PSR J2229+6114 from pulse profile fitting, and a conservative  $\theta \approx 10^\circ$  for the nearly aligned PSR J1849-0001.[23–26]

With different angle assumption mentioned above, the coupling constant distribution show in Fig. 2(a), and the combined upper bound is also showed in Fig. 2(b). A central component of our analysis is the intense magnetic environment of these targets; the surface magnetic fields ( $B_0$ ) were estimated using the standard magnetic dipole braking model[27], yielding values of  $2.03 \times 10^{12}$  G for PSR J2229+6114,  $7.5 \times 10^{11}$  G for PSR J1849-0001, and  $1.2 \times 10^{12}$  G for PSR B0531+21.[28–30]

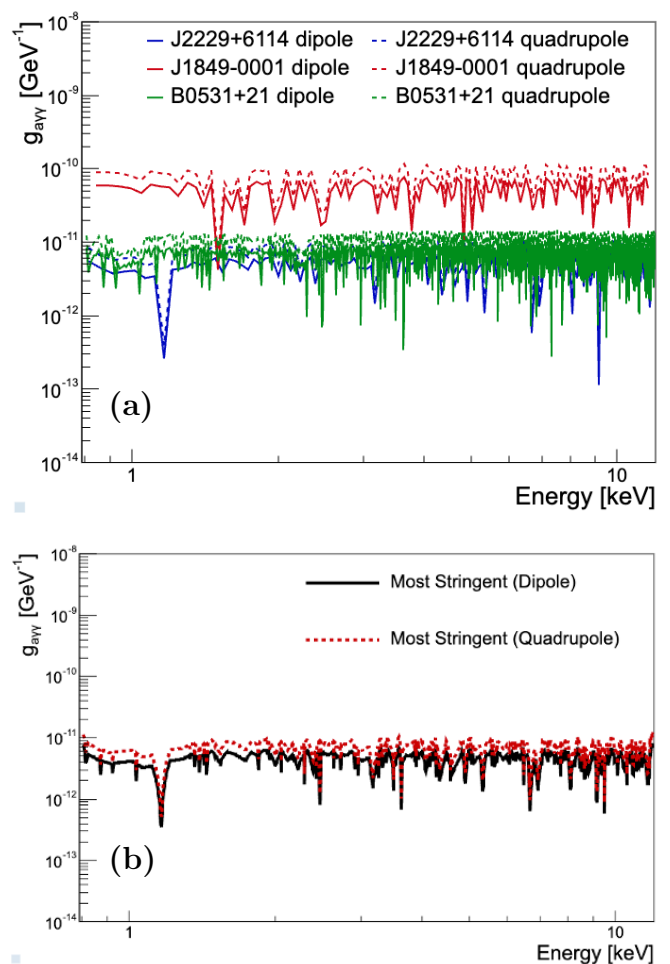


FIG. 2. Axion-photon coupling constant constraints result from J2229+6114, J1849-0001 and B0531+21 pulsar spectra (a) for different tilt angle assumption and (b) upper bound of all of the pulsar in two different magnetic field distribution.

Figure 3(a) shows the derived constraints for each pulsar and compares them with non-dark matter axion constraints near X-ray range and this result might provide new extension of the existing bounds. Figure 3(b) shows

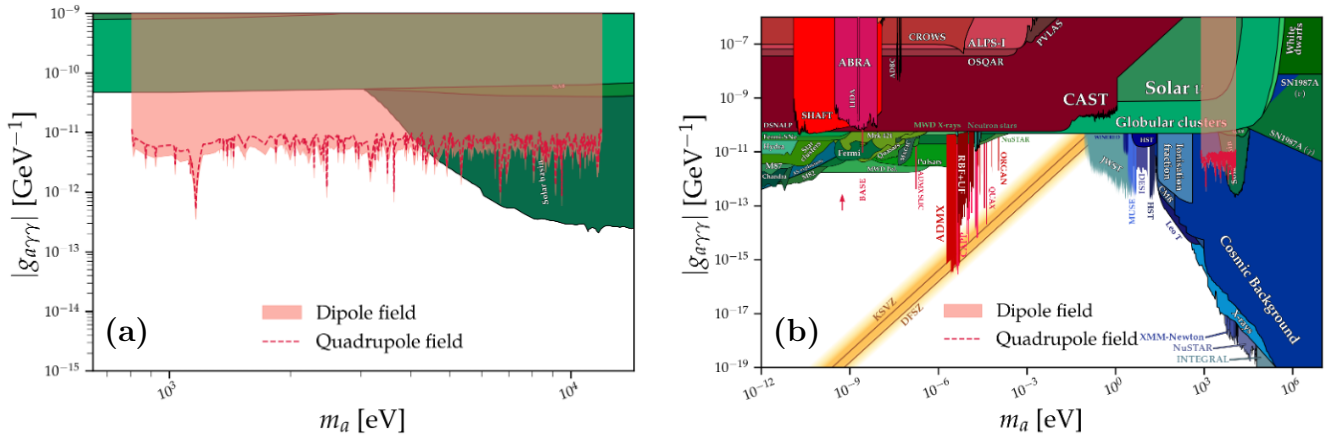


FIG. 3. Constraints on the axion-photon coupling constant  $g_{a\gamma\gamma}$  derived from NICER observations of PSR J2229+6114, PSR J1849–0001, and PSR B0531+21. (a) The derived limits compared with existing non-dark matter axion constraints in the X-ray regime. (b) The combined upper bounds across the full ALP mass range, compared against various astrophysical and cosmological dark matter constraints. All limits are calculated at the 95% confidence level.

the constraints compared with dark matter axion constraints from the astrophysical bounds.

## V. CONCLUSION

In summary, We analyzed NICER observations of three rotation-powered pulsars, PSR J2229+6114, PSR J1849–0001 and PSR B0531+21, to search for spectral signatures of photon–ALP conversion. Using a sliding-window power-law analysis, we derived constraints of  $g_{a\gamma\gamma} \sim 10^{-10} - 10^{-13} \text{ GeV}^{-1}$ , by assuming the angle of pulsar tilt and the magnetic field distribution. The PSR J2229+6114 and B0531+21 providing the strongest limit based on the assumptions. Though the study gives

us the rough story about the coupling constant, the further study toward these pulsar is still necessary. These findings highlight the potential of X-ray observations of strongly magnetized pulsars as sensitive probes of axion-like particles in the relativistic regime.

## VI. ACKNOWLEDGMENT

We thank the Institute of Physics, Academia Sinica, and the Department of Physics, National Cheng Kung University, for their support. We also acknowledge funding from the National Science and Technology Council (NSTC), Taiwan.

- 
- [1] Frank Wilczek. Problem of strong P and T invariance in the presence of instantons. *Phys. Rev. Lett.*, 40:279, 1978.
- [2] Roberto D. Peccei and Helen R. Quinn. CP conservation in the presence of pseudoparticles. *Phys. Rev. Lett.*, 38:1440, 1977.
- [3] Steven Weinberg. A new light boson? *Phys. Rev. Lett.*, 40:223, 1978.
- [4] Igor G. Irastorza and Javier Redondo. New experimental approaches in the search for axion-like particles. *Prog. Part. Nucl. Phys.*, 102:89, 2018.
- [5] Javier Redondo and Andreas Ringwald. Light shining through walls. *Contemp. Phys.*, 52:211, 2011.
- [6] S. J. Asztalos et al. Large-scale microwave cavity search for dark-matter axions. *Phys. Rev. D*, 64:092003, 2001.
- [7] Nick Du et al. Search for invisible axion dark matter with the axion dark matter experiment. *Phys. Rev. Lett.*, 120:151301, 2018.
- [8] Thomas Braine et al. Extended search for the invisible axion with the axion dark matter experiment. *Phys. Rev. Lett.*, 124:101303, 2020.
- [9] N. Crisosto et al. ADMX SLIC: Results from a superconducting LC circuit investigating cold axions. *Phys. Rev. Lett.*, 124:241101, 2020.
- [10] H Chang et al. First results from the taiwan axion search experiment with a haloscope at 19.6  $\mu\text{eV}$ . *Phys. Rev. Lett.*, 129:111802, 2022.
- [11] Paul Frederik Depta, Marco Hufnagel, and Kai Schmidt-Hoberg. Robust cosmological constraints on axion-like particles. *J. Cosmol. Astropart. Phys.*, 2020:009, 2020.
- [12] Sara Porrás-Bedmar, Manuel Meyer, and Dieter Horns. Novel bounds on decaying axionlike particle dark matter from the cosmic background. *Phys. Rev. D*, 110:103501, 2024.
- [13] V. Anastassopoulos et al. New CAST limit on the axion–photon interaction. *Nat. Phys.*, 13:584, 2017.
- [14] Klaus Ehret et al. Resonant laser power build-up in ALPS—a ‘light-shining-through-walls’ experiment. *Phys. Lett. B*, 689:149, 2010.

- [15] Mariia Khelashvili et al. Axion pulsarscope. *Phys. Rev. D*, 111:083027, 2025.
- [16] Eike Ravensburg et al. Constraining MeV-scale axion-like particles with Fermi-LAT observations of SN 2023ixf. *Phys. Rev. D*, 109:023018, 2024.
- [17] Pierluca Carenza et al. Constraints on the coupling with photons of heavy axion-like-particles from globular clusters. *Phys. Lett. B*, 809:135709, 2020.
- [18] P. S. Bhupal Dev et al. First constraints on the photon coupling of axionlike particles from multimessenger studies of the neutron star merger GW170817. *Phys. Rev. Lett.*, 132:101003, 2024.
- [19] Z. Arzoumanian et al. The Neutron Star Interior Composition Explorer (NICER): mission definition. In *Proc. SPIE*, volume 9144, page 914420, 2014.
- [20] Ronald A. Remillard et al. An empirical background model for the NICER X-ray timing instrument. *Astron. J.*, 163:130, 2022.
- [21] K. S. Cheng and L. Zhang. Multicomponent X-ray emissions from regions near or on the pulsar surface. *Astrophys. J.*, 515:337, 1999.
- [22] F. Y.-H. Wang, M. Ruderman, Jules P. Halpern, and T. Zhu. Models for X-ray emission from isolated pulsars. *Astrophys. J.*, 498:373, 1998.
- [23] Seth Gagnon et al. Chandra X-ray observations of PSR J1849-0001, its pulsar wind nebula, and the TeV source HESS J1849-000. *Astrophys. J.*, 968:67, 2024.
- [24] J. Pétri et al. Localizing the non-thermal X-ray emission of PSR J2229+6114 from its multi-wavelength pulse profiles. *Astron. Astrophys.*, 687:L13, 2024.
- [25] B. Aschenbach and W. Brinkmann. A model of the X-ray structure of the Crab Nebula. *Astron. Astrophys.*, 41:147, 1975.
- [26] R. Willingale et al. New light on the X-ray spectrum of the Crab Nebula. *Astron. Astrophys.*, 365:L212, 2001.
- [27] W. W. Macy, Jr. Pulsar magnetic axis alignment and counteralignment. *Astrophys. J.*, 190:153, 1974.
- [28] J. P. Halpern et al. PSR J2229+6114: discovery of an energetic young pulsar in the error box of the EGRET source 3EG J2227+6122. *Astrophys. J.*, 552:L125, 2001.
- [29] E. V. Gotthelf, J. P. Halpern, R. Terrier, and F. Matana. Discovery of an energetic 38.5 ms pulsar powering the gamma-ray source IGR J18490-0000/HESS J1849-000. *Astrophys. J. Lett.*, 729:L16, 2011.
- [30] M. Y. Ge et al. X-ray phase-resolved spectroscopy of PSRs B0531+21, B1509-58, and B0540-69 with RXTE. *Astrophys. J. Suppl. Ser.*, 199:32, 2012.

### Appendix A: Summary of Observations

TABLE I. Summary of the NICER pulsar observations and magnetospheric parameters. The surface magnetic fields ( $B_0$ ) are estimated using the standard dipole braking model [27], and the observation IDs (ObsID) represent the cleaned data segments used for spectral fitting.

Pulsar Name	Surface Magnetic Field (G)	Energy Range (keV)	ObsID	Exposure Time (s)
B0531+21	$1.2 \times 10^{12}$	[0.805, 11.995]	1013010147	24069
			1013010125	20543
			1013010126	19892
			1013010150	15921
			1013010148	15476
			1013010146	14961
			1013010152	12961
			1013010143	11822
			1013010144	11411
			1013010145	11307
J1849-0001	$7.5 \times 10^{11}$	[1.550, 9.230]	3536040701	11306
			3536041102	9740
			3536040101	9451
			3536040806	8315
			3536040201	7686
			3536040901	7206
			3536040802	7098
			3536041002	6868
			3536040902	6040
			3536040301	5989
J2229+6114	$2.3 \times 10^{12}$	[0.915, 5.525]	2579050301	30362
			2579050914	24539
			2579050401	22299
			2579050202	19110
			2579050302	19092
			2579051210	18607
			2579051101	18530
			2579050101	18176
			2579050502	14995
2579050606	12065			